A Study on the Corrosion and Tribocorrosion Behavior of Al-30 Vol.% B₄C Composite Produced by Mechanical Milling and Hot Pressing

H. Mindivan (ORCID)

The present work aims to study the corrosion and tribocorrosion behaviors of pure Al and Al-30 vol.% B₄C fabricated by a combination of mechanical milling and hot-pressing processes. Structural analysis and phase composition of the pure Al and the Al-30 vol.% B₄C composite were evaluated by field emission-scanning electron microscopy and x-ray diffractometry, respectively. The corrosion behavior was investigated using electrochemical impedance spectroscopy and potentiodynamic polarization in a 3.5 wt.% NaCl solution. Tribocorrosion tests were performed under an open-circuit potential in the same solution with a ball-on-flat configuration, and Al₂O₃ balls were used. Electrochemical studies revealed that the composite with 30 vol.% B₄C presented lower resistance to corrosion as compared to the pure Al evidenced by a decrease on the corrosion potential, an increase on the corrosion current density and a smaller diameter of the semicircle presented in the Nyquist diagram. The results from the potentiodynamic polarization measurements showed that pure Al corroded at 58% slower rate when compared to the corrosion rate of Al-30 vol.% B₄C composite. However, tribocorrosion tests showed that B₄C particle addition to the Al matrix decreased the wear volume of the resulted composite from 1.48 to 0.03 mm³.

1. Introduction

Aluminum (Al) and its alloys have been gathering a lot of interest in the aircraft, automotive, construction, packaging, electronics and military industries due to their high strength to weight ratio as well as their environmental resistance to degradation in many corrosive media, including atmospheric environments, fresh and salt waters, and in many chemicals and chemical solutions (Ref 1). When exposed to air, Al alloy does not oxidize progressively because an inert and protective oxide film forms on the surface and seals the metal from the environment. The mechanical strength is strongly required in the actual use. The high performance tribological applications, however, is also important when using them in corrosive medium, such as valves, impellers and pumps. The tribocorrosion properties of monolithic Al alloys were discussed (Ref 2). It showed that the material removal was mainly by a high plastic deformation around the wear track and ductile characteristic of the Al alloy. As a result, a poor tribocorrosion resistance and low seizure loads prevent a direct use of monolithic Al alloys due to the intensive friction and mechanical loading. The corrosion and tribological phenomenon impose a huge damage to economy and industry. It has been reported that 10% of the material degradation in engineering parts occurs due to corrosion, while 30% is due to abrasion, 15% is due to adhesion and 10% is due to tribocorrosion (Ref 3).

Silicon carbide (SiC), Aluminum oxide (Al₂O₃) and Boron Carbide (B₄C) are widely used as potential hard ceramic reinforcements in Al matrix composites. Although it is expensive compared to other ceramic types, B₄C is preferred as a reinforcement material due to its low density (2.51 g/cm³) (Ref 4) that is lower than that of Al₂O₃ or SiC, high hardness (> 30 GPa) and wear resistance, high chemical inertness (Ref 4, 5) and neutron absorption capacity (Ref 6). Al-B₄C metal matrix composites (MMCs) can be an attractive candidate for neutron absorber materials to fabricate the inside basket of transport and storage casks for spent nuclear fuels in the nuclear industry (Ref 7). Adding of B₄C particles to the Al matrix alloy through various composite production techniques to enhance the mechanical property (hardness and wear resistance) could also significantly decrease its corrosion resistance (Ref 8). Han et al. (Ref 4) reported that Al-B₄C composites showed lower corrosion resistance than Al alloys. Moreover, the electrochemical resistance of such composites decreased with increasing the B₄C content in the produced composites. It was found that the galvanic corrosion of Al-B₄C composites was limited by the slow rate of oxygen reduction at the B₄C particles which did not promote the galvanic corrosion (Ref 9). It was reported that Al-B₄C composites exhibited lower corrosion rates when exposed to the NaCl solution (Ref 10). Alaneme and Olubambi (Ref 11) studied the corrosion properties of Al alloy reinforced with Al₂O₃ and rice husk ash in a 3.5% NaCl solution. It was reported that the composite with a higher weight percentage of Al₂O₃ with higher density (3.9 g/cm³) exhibited the enhanced corrosion resistance compared to the composite with a higher weight percentage of rice husk with lower density (0.3 g/cm³). Ashraf et al. (Ref 12) demonstrated Al-30Fe₃O₄-20SiC composite had the excellent corrosion resistance in simulated

H. Mindivan, Department of Mechanical Engineering, Bilecik Şeyh Edebali University, Bilecik, Turkey. Contact e-mail: harun.mindivan@bilecik.edu.tr.

seawater media. Abu-Warda et al. (Ref 13) studied the corrosion properties of A6005-TiB$_2$ nanocomposites in a 3.5% NaCl solution. It was reported that mechanical alloying processing and 5 wt.% nano-TiB$_2$ addition did not produce significant negative effects on its corrosion resistance.

It has been expressed that Al-B$_4$C composites produced by powder metallurgy (P/M) offer significant advantages compared with conventional casting because of its low process temperature, which presents less interaction between the Al and the B$_4$C (Ref 14, 15). An additional advantage of P/M process is its low processing costs along with its high versatility. But still, to obtain a defect-free microstructure with an enhanced mechanical property, it is essential for the particles to be uniformly dispersed into metal matrices (Ref 15). However, due to the poor wettability in Al-B$_4$C system, and a large surface-to-volume ratio, the uniform dispersion of fine B$_4$C particles in the Al matrix is an important problem for processing of composites. Hot pressing is a P/M process that combines the pressing and sintering steps simultaneously and therefore, provides a simpler production route with better mechanical and electrochemical properties as compared to the conventional techniques (Ref 16). Because of this, a P/M process involving a hot-pressing step is accounted as an excellent technique for the consolidation of Al-B$_4$C powders (Ref 14). It should be noted that, a study has focused on the both corrosion and tribocorrosion properties of Al composites with 20 vol.% B$_4$C prepared through stir casting approach (Ref 8). This work aims to develop a fundamental understanding of Al and Al-B$_4$C composite, their structure and their corrosion and degradation mechanisms during tribocorrosion. Al was chosen as the matrix for its high corrosion resistance and passivity in 0.6 M NaCl aqueous solution, while B$_4$C particles were chosen because they were stable compounds, which were not dissolved by aqueous alkalis and mineral acids (Ref 10). Since the in-service properties of Al composite with 30 vol.% B$_4$C fabricated through a cost-effective processing technique based on P/M route is highly essential besides mechanical properties in order to expand their potentiality under wear and corrosive conditions such as nuclear, offshore, aircraft and military components (Ref 6, 17, 18), it would therefore be of interest to evaluate microstructure, hardness, corrosion and tribocorrosion behavior of Al matrix composite with 30 vol.% B$_4$C in the as-received state against the threat of wear and corrosion.

2. Materials and Methods

High purity Al powders (99.9% purity) with average particle size of 27 μm were used as the matrix alloy. Angular shape B$_4$C particles (Grade HS, HC Starck, Berlin, Germany) with an average size of 3.5 μm were added as reinforcement. To obtain uniform particulate distribution, powders were milled using a planetary ball mill. The tungsten carbide milling vial and balls were selected as the milling medium. Milling parameters were selected as follows: ball to powder ratio 10:1, planetary-disk rotation speed 400 rpm and with stearic acid (CH$_3$ (CH$_2$) 16CO$_2$H) addition as process control agent (PCA). Al-30 vol.% B$_4$C powders, which were milled for 24 h, were uniaxially cold-pressed in a steel mold of 30 mm in diameter with an axial pressure of 700 MPa. Since the hard B$_4$C particles restricted the deformation of the composite (Ref 19), the mixture were then hot-pressed at 773 K with a pressure of 1600 MPa in a steel mold for 1 h and allowed to cool at atmospheric temperature, so discs with 30 mm diameter and 10 mm thickness were obtained. The pure Al has an exact hot consolidation process similar to composite as a reference.

Microstructural evaluations were carried out by a field emission-scanning electron microscopy (FE-SEM) equipped with the energy dispersive x-ray (EDX) spectroscopy and an
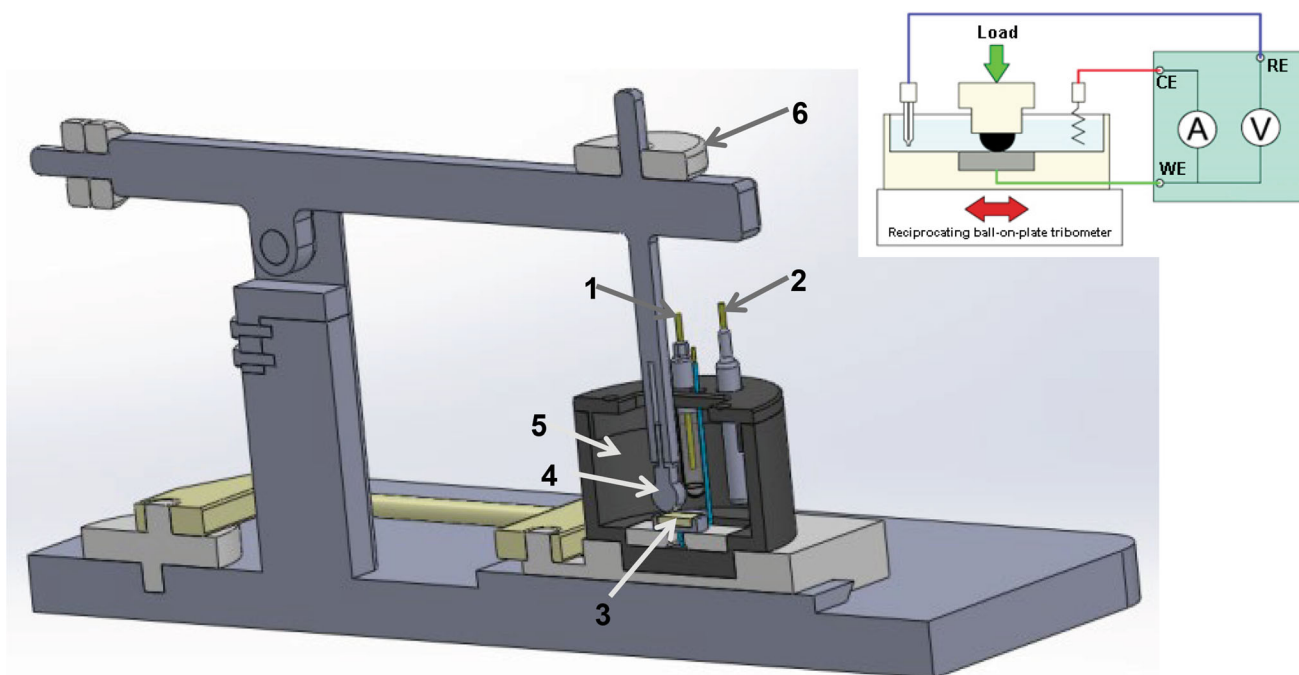
Fig. 1 Schematic view of reciprocating tribometer coupled with electrochemical cell used in this study: (1) Reference Electrode (RE), (2) Counter Electrode (CE), (3) Working Electrode (WE), (4) Al$_2$O$_3$ ball, (5) Electrolyte, (6) Load

	X500	X1000	X1500
Pure Al			
Al-30 vol.% B$_4$C			
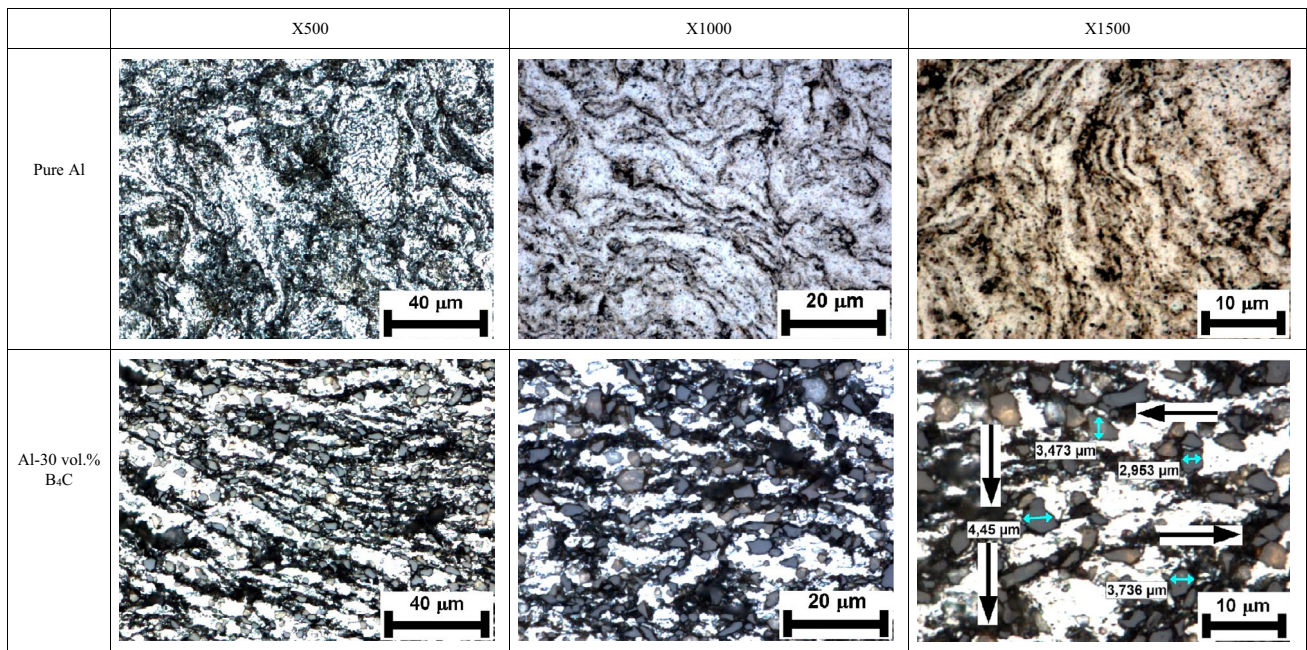
Fig. 2 Low and high magnification OM photographs of the pure Al and Al-30 vol.% B$_4$C composite. The arrows show some of the micro-voids present in the composite

Table 1 The void content, Knoop hardness and density test results

B$_4$C content, vol.%	Void content, %	Knoop hardness, HK$_{0.5}$	Experimental density, g/cm^3
0	1.8	181 ± 7.5	2.65
30	2.4	214 ± 15	2.58

optic microscope (OM), respectively. The phase identification was carried out using x-ray diffraction (XRD) performed at 2θ sweeps from 10 to 90° with a Cu K$_\alpha$ (λ = 1.54 A°) radiation source, and the crystallite size was determined by applying the Scherrer Eq 1 (Ref [20]).

$$L = (K.\lambda)/(\beta. \cos\theta) \qquad (Eq\ 1)$$

where L is the crystallite size, K is a constant related to crystallite shape, β is the full width at half maximum (FWHM), λ is the wave length and θ is the peak position. The hardness measurement was accomplished using Knoop diamond indentation under a 500 g load for a period of 15 s. The obtained results were the average of five measurements. The theoretical density of the pure Al and the composite with 30 vol.% B$_4$C was computed using rule-of-mixture, while experimental density was evaluated using helium-gas-based pycnometer technique. More detail regarding the void content calculation used in this work has been reported elsewhere (Ref [21]).

The electrochemical corrosion response of the samples was detected by means of a Gamry model PCI4/750 Potentiostat/ Galvanostat controlled by a computer with DC105 corrosion analysis software at room temperature using a three-electrode cell, consisting of a working electrode, a saturated calomel electrode and a platinum electrode. The potentiodynamic polarization (PDP) measurements were conducted in 100 ml solutions of 3.5 wt.% NaCl by sweeping the potential from cathodic to anodic direction at a constant scan rate of 1 mV s^{-1}, starting from $-$ 1.2 up to $-$ 0.60 V. Electrochemical impedance

spectroscopy (EIS) was conducted at the frequency range from 100 kHz to 0.002 Hz. The impedance spectra were analyzed in 3.5 wt.% NaCl at the open-circuit potential (OCP). Prior to electrochemical tests, the samples were allowed to stabilize to obtain a stable OCP. Finally, the corroded surfaces were analyzed by FE-SEM/EDX in order to identify the morphologies of the corrosion surfaces.

Tribocorrosion experiments were conducted in a three-electrode chemical cell containing 25 ml of 3.5 wt.% NaCl solution installed on a linear reciprocating ball-on-plate configuration (Fig. 1). For the tribocorrosion tests, machined samples of $5 \times 10 \times 20$ mm were soldered to a wire for electrical contact and embedded in an epoxy resin holder. Before the tribocorrosion tests, the surface of samples was then abraded up to 1200 mesh emery paper, mechanically polished down to 1 µm alumina paste to reach an average surface roughness (Ra) of 0.08 ± 0.01 µm. The testing sample serves as the working electrode (WE), and its potential is monitored using a Gamry model PCI4/750 Potentiostat/Galvanostat. The reference electrode (RE) was an Ag/AgCl, and the counter electrode (CE) was a platinum rod. Hubner and Wranglerr reported that pits do not nucleate on Al in the OCP condition (Ref [22]). Therefore, reciprocating sliding tests were carried out under OCP conditions. The OCP was recorded before, during and after reciprocation sliding contact with the Al$_2$O$_3$ ball of Ø = 10 mm. The tribocorrosion tests consisted of the three steps: (1) OCP stabilization for 600 seconds before sliding; (2) OCP variation for 2700 seconds during sliding; (3) OCP stabilization
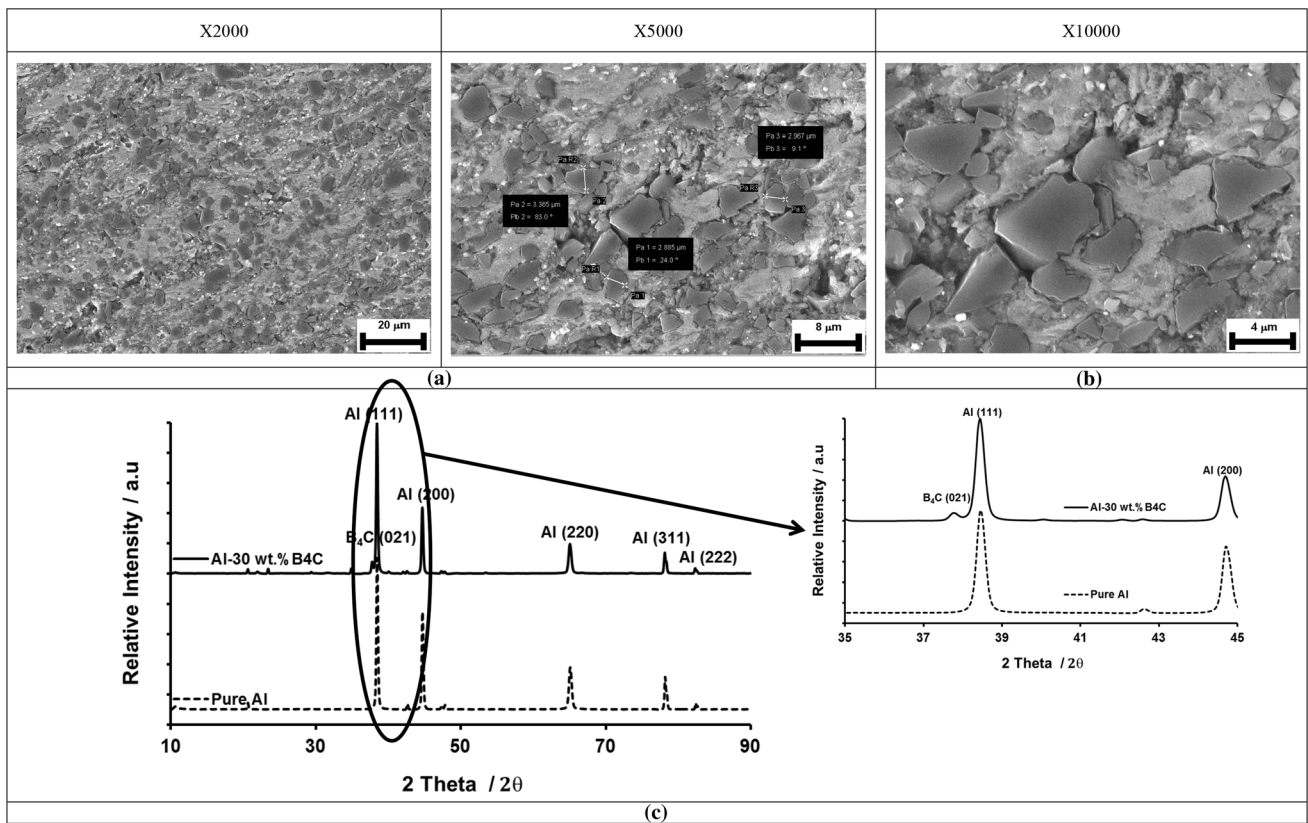
Fig. 3 (a) Low- and (b) high-magnification FE-SEM photographs showing the uniform distribution of B_4C particles in the Al-30 vol.% B_4C composite and (c) XRD patterns of pure Al and Al-30 vol.% B_4C composite.
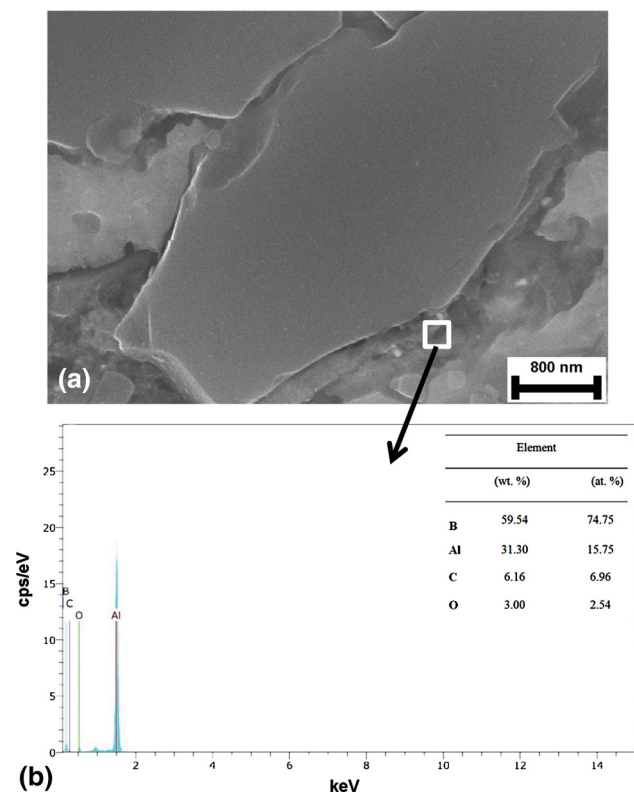

Fig. 4 (a) FE-SEM photograph showing the interface of Al-30 vol.% B_4C composite and (b) EDX spectra showing the elements present at the interface of Al-30 vol.% B_4C composite
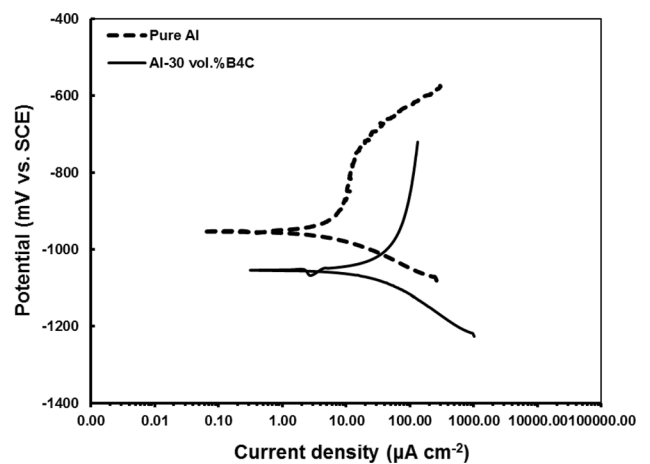

Fig. 5 Potentiodynamic polarization curves of pure Al and Al-30 vol.% B_4C composite recorded in 3.5 wt.% NaCl solution

for 600 seconds after sliding. Tests were performed under a load of 5 N, a stroke length of 11.5 mm, a speed of 1.9 cm s^{-1} and a total sliding distance of 57.5 m. During the test, an exposure area of ~ 2 cm^2 was exposed to the corrosive electrolyte. The coefficient of friction (COF) was recorded by the load cell. After tribocorrosion tests, the wear scars were cleaned in acetone and the contact surfaces of wear scars were examined by a FE-SEM. Total material loss rates were determined by measuring the 2D cross-sectional area profile
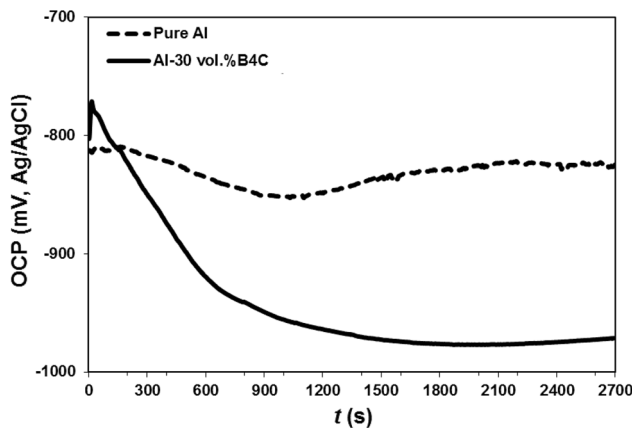
Fig. 6 OCP time response of pure Al and Al-30 vol.% B₄C composite recorded in 3.5 wt.% NaCl solution
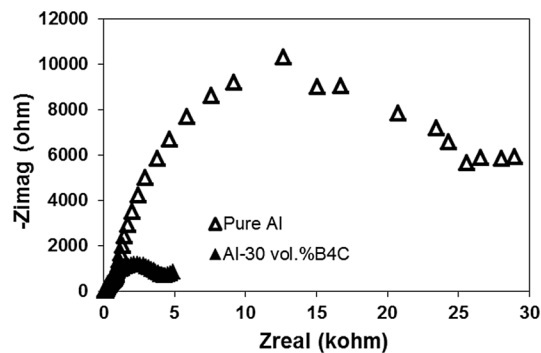
Fig. 7 Nyquist plots of pure Al and Al-30 vol.% B₄C composite recorded in 3.5 wt.% NaCl solution

of the wear scars (in three locations) by using a contact profilometer (Mitutoyo Surtest SJ-400) and converting this to a wear volume by taking account of the scar length. By the end of the OCP tribocorrosion tests, optical densities of test solution were measured using a UV-spectrophotometer (T80 UV/VIS spectrometer P6 Instruments Ltd.) in order to determine the density of their wear products in the test solution. Freshly prepared 3.5 wt.% NaCl solution was analyzed as the reference to evaluate the optical densities of solutions. After the spectrophotometric measurement of freshly prepared 3.5 wt.% NaCl solution by using fix visible light (wave length: 202 nm), the data obtained were automatically adjusted to zero in order to determine the optical densities of the test solutions utilized in the OCP tribocorrosion tests.

3. Results and Discussion

The microstructure of pure Al shows almost pore-free (Fig. 2). In hot press process, when the temperature is below the melting point of Al, applied pressure can deform the soft Al particles and the space between particles is reduced, causing a reduction in voids (1.8%). In the case of Al-30 vol.% B₄C (Fig. 2), since the hard B₄C particles suppress the deformation there are micro-voids (2.4%) in the approximate size of 3-4 μm in the microstructure of hot-pressed composite. The void content, Knoop hardness and density test results are given in Table 1. Since the Knoop hardness of the Al-30 vol.% B₄C composite was found to be almost 18% greater as compared to the pure Al, it can be concluded that the production process was carried out perfectly (Ref 23). On the other hand, the density was observed to decrease with the existence of B₄C particles

	Low Magnification (X250)	High Magnification (X1000)	EDX Analysis			
Pure Al			Element (wt. %)	X	Y	Z
			Al	53.90	57.09	57.49
			O	42.50	40.30	40.75
			Mg	-	1.49	0.58
			Cl	3.60	0.86	1.12
			Na	-	0.26	0.06
Al-30 vol.% B₄C			Element (wt. %)	X	Y	Z
			B	1.44	22.67	-
			C	16.99	18.92	-
			O	59.65	43.51	68.30
			Al	19.91	11.39	30.47
			Na	2.01	0.76	1.24
			Mg	-	2.76	-

Fig. 8 Low- and high-magnification FE-SEM photographs of the pure Al and Al-30 vol.% B₄C composite after the corrosion tests

which is thought to be related to the relatively lower density of B_4C (2.52 g/cm^3) compared to Al (2.7 g/cm^3) (Ref 17). The crystallite sizes of the pure Al and Al-30 vol.% B_4C composite were measured as 47 nm and 38 nm, respectively. A decrease in the crystallite size value was observed with addition of B_4C particles to the Al matrix. The decreased value recorded in the Al-30 vol.% B_4C composite could be as a result of the milling process used to achieve effective dispersion of the B_4C particles within the Al matrix. On the other hand, during hot deformation the B_4C particles can stimulate the dynamic recrystallization nucleation, restrain the grain growth and reduce the preferential orientation of the Al grains (Ref 24).

Figure 3 depicts the distribution of B_4C particles in the Al matrix. It can be observed that fabrication of this composite via hot press process lead to reasonably uniform distribution of B_4C particles in the Al matrix and minimum clustering or agglomeration of the B_4C particles (Fig. 3a). However, micro-voids observed at the particle/matrix interface of the composite with 30 vol.% B_4C can be trapped between agglomerated B_4C particles and survive even after hot press process, as shown in Fig. 3(b). The XRD patterns of the pure Al and Al-30 vol.% B_4C composite are given in Fig. 3(c). Al peaks were identified at 2θ angle of 38.43°, 44.69°, 65.04°, 78.18º and 82.39°. The miller indices of these peaks are found out to be (111), (200), (220), (311) and (222), respectively. B_4C peak can be seen at a diffraction angle of 37.74°. However, it was observed that there was a decrease in the height of Al peaks in the composite with 30 vol.% B_4C due to structural refinement. From the XRD patterns, it can be confirmed that only Al and B_4C peaks are

found and no other intermetallic phases were formed after 24 hours milling. Similar results were found in the various literatures (Ref 5, 14, 17). Figure 4 shows the SEM micrograph of Al-B_4C interface with EDX result in the Al-30 vol.% B_4C composite. Small B_4C particles ($\leq$ 3.5 μm) tended to debond by interfacial decohesion, resulting in micro-voids. The EDX spectrum revealed the presence of the elements Al, B and C in the Al-B_4C interface. The EDX result is well consistent with the XRD results shown in Fig. 3(c).

The corrosion properties of the pure Al and the Al-30 vol.% B_4C composite were examined using the PDP technique. To achieve the equilibrium potential, the area of $\sim$ 0.25 cm^2 of samples was immersed in the solution of 3.5 wt.% NaCl for about 2700 seconds. As seen in the Fig. 5, the pure Al shown higher cathodic current density at the given potential compared to Al-30 vol.% B_4C composite. But, pure Al exhibited smaller anodic current density compared to Al-30 vol.% B_4C composite. The oxidation of Al and evolution of hydrogen gas/oxygen reduction occur at the anode and cathode, respectively. The polarization curves as represented in Fig. 5 demonstrate a decrement in corrosion performance of monolithic Al by the incorporation of B_4C particles as it indicated by reduction in corrosion potential (from – 954 to – 1050 mV), increase in corrosion current (from 2.64 $\times$ 10^{-6} to 6.26 $\times$ 10^{-6} A/cm^2) and increase in corrosion rate (from 93.68 $\times$ 10^{-3} to 223.00 $\times$ 10^{-3} mmpy). Pure Al corrodes at 58% slower rate when compared to the corrosion rate of Al-30 vol.% B_4C composite.

To further probe the corrosion results, EIS was measured for the pure Al and its composite in 3.5 wt.% NaCl solution. Before the EIS tests, the evolution of the OCP values of the pure Al and Al-30 vol.% B_4C composite with time is presented in Fig. 6. The OCP value can be used to measure the corrosion tendency of the sample in an aqueous solution, and a higher OCP value means lower corrosion tendency (Ref 25). It is inferred from Fig. 6, that the OCP value of the Al-30 vol.% B_4C composite was lower compared to the pure Al during the entire corrosion cycle. It is observed that the OCP is stabled at $\sim$ – 824 and $\sim$ – 976 mV for the pure Al and Al-30 vol.% B_4C composite, respectively.

The poor corrosion performance for the Al-30 vol.% B_4C composite is also determined by the EIS results shown in Fig. 7. As can be observed in the Nyquist plots (Fig. 7), the pure Al presented a noble corrosion behavior with a larger diameter of the semicircle when compared to the Al-30 vol.% B_4C composite. From these results, it is evident that introduction of B_4C particles into Al matrix can break the continuity of the protective Al oxide layer, increasing a possibility of blisters on the composite surface.

Figure 8 shows the surface morphologies of the pure Al and Al-30 vol.% B_4C composite which are immersed into chloride-containing solution. Uneven layers of corrosion products were formed on the surface of the pure Al. In NaCl solution, the corrosion reaction of Al can be described as follows (Ref 26):

$$4Al + 3O_2 + 6H_2O \rightarrow 4Al(OH)_3 \qquad (Eq\ 2)$$
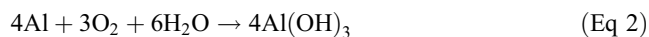
The corrosion product Al $(OH)_3$ may also undergo additional reactions to form Al_2O_3:

$$4Al(OH)_3 \rightarrow 2Al_2O_3 + 6H_2O \qquad (Eq\ 3)$$
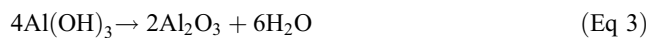
It was found that the Al can react with other elements to produce Al $(OH)_3$ or Al_2O_3 according to the Eqs 2 and 3. It is worth noting that the EDX examination on the selected spots
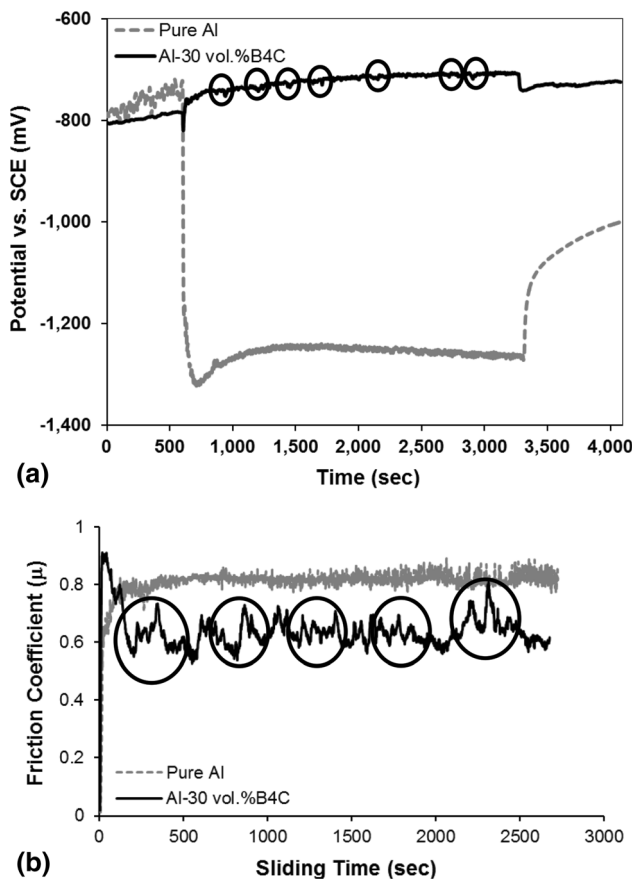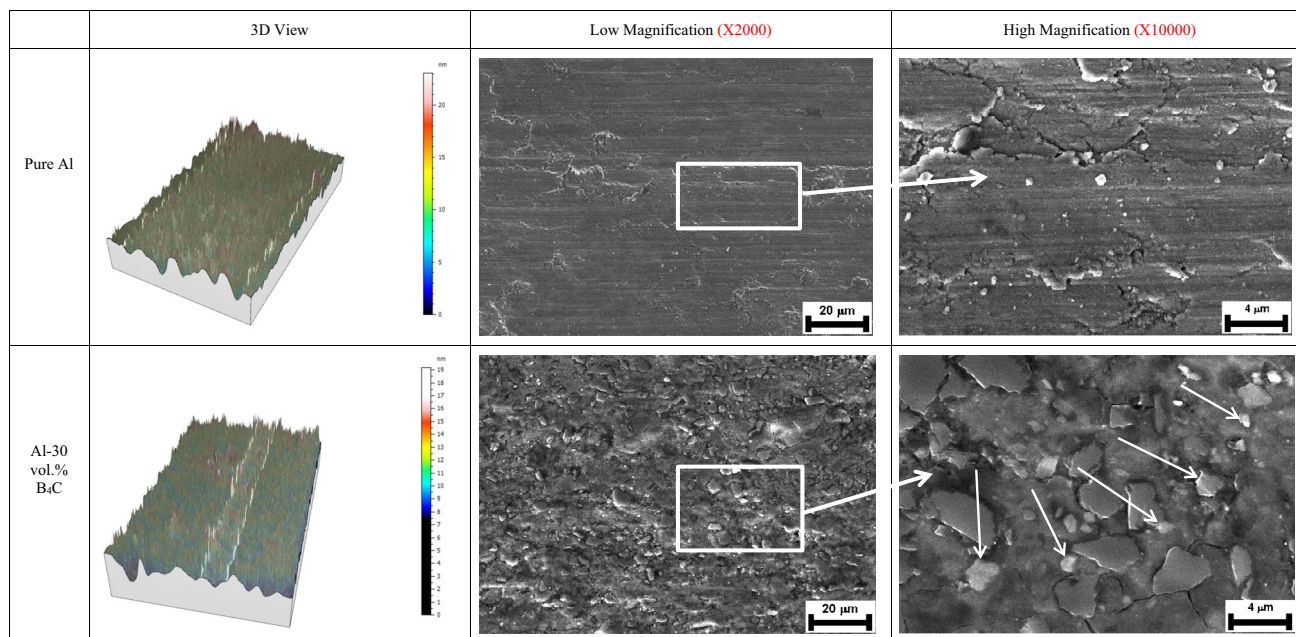

Fig. 9 (a) OCP an (b) COF monitoring for pure Al and Al-30 vol.% B_4C composite during the OCP tribocorrosion tests

Fig. 10 3D view, low and high magnification FE-SEM photographs of the wear tracks of the pure Al and Al-30 vol.% B$_4$C composite after the OCP tribocorrosion tests. The arrows show partially oxidised wear debris emerged from the worn surface
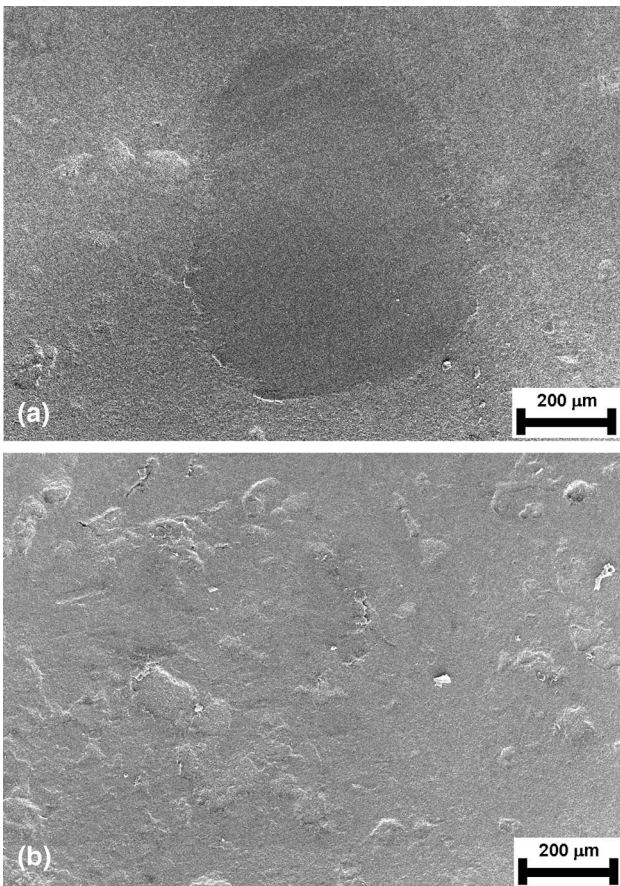
Table 2   Tribocorrosion test results

B$_4$C content, vol.%	Optical density, a.u.	Friction coefficient, COF	Wear volume, mm^3
0	1.87 ± 0.02	0.81 ± 0.05	1.48 ± 0.03
30	1.55 ± 0.01	0.63 ± 0.03	0.03 ± 0.01

shown in Fig. 8 detected layers consisting of rich in Al oxides. Chlorides were observed in the three spots (*X*, *Y* and *Z*), and chloride and Al oxides were detected near the surface denoting penetration of chlorine through the pure Al. It was noted that the corrosion rate of the high purity Al samples with a range of grain sizes, from ∼ 100 to ∼ 2000 μm, produced using different processing routes tended to decrease with decreasing grain size, in neutral NaCl solutions, that serves to decrease corrosion rate through faster growth of a protective oxide (Ref 27). It is generally claimed that fine-grained Al alloys exhibit improved resistance to pitting, decreased cathodic kinetics, better results in mass-loss testing, and in some circumstances, better resistance to stress corrosion cracking (SCC). A different view, that corrosion rate increases or decreases as grain size decreases for Al samples depending on whether grains were equiaxed or columnar, has also been presented (Ref 28). Also apparent from this work, however, is that chloride ions show a strong attack to passive film, resulting in facilitating the dissolution of the protective passive film in the pure Al. The research of Durai et al. showed that the milling procedure improves the composite corrosion resistance in passive conditions (Ref 29). In this study, it has been found that the milled Al-Zn/ Al$_2$O$_3$ composite offers higher corrosion resistance compared to unmilled Al-Zn/ Al$_2$O$_3$ composite. The corrosion behavior of MMCs depends on various factors like compositions of the alloy used and the reinforcing particles, their size and distribution in the matrix, and the nature of the interface

between the matrix and the reinforcement (Ref 26, 29). In the present case, the Al-30 vol.% B$_4$C composite were not attacked by the pitting corrosion since there were no severe pits on the composite surface as shown in Fig. 8. Besides, the presence of blisters observed on the composite surface indicated that the localized dissolution happened at the Al/B$_4$C interfacing beneath the oxide layer (Ref 10). The Al1100-16 vol.% B$_4$C composites fabricated by Han et al. (Ref 4) have showed the higher corrosion rate owing to the B$_4$C reinforced into Al matrix than corresponding monolithic Al1100 alloy. These observations indicate that addition of B$_4$C particles to the monolithic Al can reduce the corrosion resistance in NaCl solution, which was reflected by the polarization and impedance measurements.

The evolution of the OCP as a function of time before, during and after the sliding motion is illustrated in Fig. 9 for the pure Al and Al-30 vol.% B$_4$C composite, along with their corresponding COF values obtained during the OCP tribocorrosion tests. In the pure Al, when sliding started, OCP values dropped down sharply (from − 740 to − 1310 mV), it means that the native passive oxide film was damaged due to the shear stress generated by the contact between the ball and the surface under a test load of 5 N. Galvanic corrosion would occur due to the differences in potential cathode/anode (Ref 30, 31). Consequently, in the sliding track fresh active pure Al becomes exposed to the solution, which causes the drop in the OCP (Ref 32–35). The pure Al showed low fluctuations in the OCP, but

Fig. 11 FE-SEM photographs of the Al2O3 balls sliding against (a) Al-30 vol.% B4C composite and (b) pure Al

The FE-SEM micrographs of worn surfaces after tribocorrosion tests are shown in Fig. 10. In the case of pure Al, a wide sliding track including excessive plastic plowing and cutting was observed along the sliding direction (Fig. 10). This could be attributed mainly to the plastic deformation by the abrading action of the Al_2O_3 ball at high Hertzian contact pressures (562 MPa) under a test load of 5 N, that was higher than the yield strength of the monolithic Al (approx. 167 MPa (Ref 35)). The degree of surface damage in the wear track of the Al-30 vol.% B_4C composite was shown to be lower in comparison with the worn surface of the pure Al (Fig. 10). Besides, due to the lower hardness of the Al matrix than the B_4C particles, partially oxidized wear debris (marked with arrows) emerged from the worn surface were kept between the B_4C particles. Since the wear debris were entrapped between the B_4C particles, the optical density obtained from the Al-30 vol.% B_4C composite in the tribocorrosion test solution was fewer as compared to the pure Al (Table 2). In a tribocorrosion work by Toptan et al. (Ref 8), an increase on the OCP values of Al-B_4C composites fabricated through stir casting technique was occurred due to the accumulated wear debris that acted as a protective layer was reported. As sliding continued, when the Al_2O_3 ball met a protruded B_4C particle, abrupt fluctuations (marked with circles) were recorded on the OCP and COF values as illustrated in Fig. 9. When the Al_2O_3 ball slided against the Al-30 vol.% B_4C composite, almost circular scar was obvious on the worn surface of Al_2O_3 ball (Fig. 11a). However, the corrosion products developed on the worn track were transferred on the worn surface of the Al_2O_3 ball after sliding against the pure Al (Fig. 11b). Therefore, the pure Al presented relatively stable OCP and COF values against the variation of the sliding time (Fig. 9).

4. Conclusion

In this paper, Al matrix composite with 30 vol.% B_4C was successfully prepared by a combination of mechanical milling and hot-pressed sintering techniques. The following results are obtained:

- Microstructural studies conducted on the composite with 30 vol.% B_4C indicated that the distribution of B_4C particles was reasonably uniform in the Al matrix while small B_4C particles (≤ 3.5 μm) tended to debond by interfacial decohesion, resulting in micro-voids.
- When compared to the pure Al, the Knoop hardness of the composite was namely about 18% higher due to the dispersion of hard B_4C particles.
- The composite with 30 vol.% B_4C presented lower resistance to corrosion as compared to the pure Al evidenced by a decrease on the corrosion potential, an increase on the corrosion current density and a smaller diameter of the semicircle presented in the Nyquist diagram. The results from the potentiodynamic polarization measurements showed that pure Al corroded at 58% slower rate when compared to the corrosion rate of Al-30 vol.% B_4C composite.
- The composite with 30 vol.% B_4C exhibited a reduction of up to 98% in the wear volume loss value as compared to the pure Al, indicated a better resistance to wear in 3.5 wt.% NaCl solution.

did not exhibit big local increments and decrements. Once the sliding was stopped, the OCP progressively increased due to the partially repassivation on the surface in the wear track and did not reach the initial OCP. However, an opposite behavior was observed for the Al-30 vol.% B_4C composite. When sliding started, instead of decreasing, the OCP slightly increased to the positive direction abruptly and then fluctuated around a characteristic value until the end of the friction test. At the end of sliding, the OCP decreased from − 709 to − 730 mV. Initial OCP after immersion of the pure Al in the electrolyte was more positive than in the case of composite with 30 vol.% B_4C. However, the recorded OCP after the start of sliding was higher for the Al-30 vol.% B_4C composite compared with the pure Al. Besides, the variation of COF of pure Al and Al-30 vol.% B_4C composite is shown in Fig. 9(b). Friction coefficient of the Al-30 vol.% B_4C composite started off from a high value and decreased with sudden fluctuations at certain time intervals (marked with circles). In contrast to the Al-30 vol.% B_4C composite, the pure Al reached a steady state regime and showed a stable friction behavior. The COF was high for the pure Al when compared with the Al-30 vol.% B_4C composite. The reduction in COF is the cause of the presence of very hard B_4C particles in Al matrix (Ref 36, 37) and prevention of direct contact of soft Al matrix into Al_2O_3 ball. The composite with 30 vol.% B_4C was mainly in contact with the Al_2O_3 ball due to the load bearing effect of the hard B_4C particles.

- The Al-30 vol.% B$_4$C composite showed a decrease in the optical density and COF values along with an increase in the OCP values throughout testing time compared to the pure Al.

References

1. Metal Handbook. Part II. Properties and Selection, Aluminum (American Society for Metals. Metals Park, 1985)
2. U. Saglam, M. Baydogan, H. Mindivan, E.S. Kayali and H. Cimenoglu, Influence of Retrogression and Reageing on Mechanical and Corrosion Properties of 7039 Aluminium Alloy, *Z. Metallkd.*, 2004, **95**, p 14–17.
3. J.-P. Celis and P. Ponthiaux, Testing tribocorrosion of passivating materials supporting research and industrial innovation: handbook, *Testing Tribocorrosion of Passivating Materials Supporting Research and Industrial Innovation: Handbook.* J.-P. Celis, P. Ponthiaux Ed., W.S. Maney & Son Ltd., Leeds, 2012, p 1–13.
4. Y.M. Han and X.-G. Chen, Electrochemical Behavior of Al-B$_4$C Metal Matrix Composites in NaCl Solution, *Material*, 2015, **8**, p 6455–6470.
5. S. Chand and P. Chandrasekhar, Influence of B$_4$C/BN on Solid Particle Erosion of Al6061 Metal Matrix Hybrid Composites Fabricated Through Powder Metallurgy Technique, *Ceram. Int.*, 2020, **46**(11), p 17621–17630.
6. Y. Jung, M. Lee, K. Kim and S. Ahn, ^{10}B(n, α)7Li Reaction-Induced Gas Bubble Formation in Al-B$_4$C Neutron Absorber Irradiated in Spent Nuclear Fuel Pool, *J. Nucl. Mater.*, 2020 https://doi.org/10.1016/j.jnucmat.2020.152077
7. Y.T. Zhou, Y.N. Zan, Q.Z. Wang, B.L. Xiao, Z.Y. Ma and X.L. Ma, Grain Boundary Segregation of Alloying Cu Induced Intergranular Corrosion of B4C–6061Al Composite, *Mater. Charact.*, 2021 https://doi.org/10.1016/j.matchar.2021.110930
8. F. Toptan, A.C. Alves, I. Kerti, E. Ariza and L.A. Rocha, Corrosion and Tribocorrosion Behaviour of Al-Si–Cu–Mg Alloy and Its Composites Reinforced with B4C Particles in 0.05 M NaCl Solution, *Wear*, 2013, **306**, p 27–35.
9. H. Ding and L.H. Hihara, Electrochemical Examinations on the Corrosion Behavior of Boron Carbide Reinforced Aluminum-Matrix Composites, *J. Electrochem. Soc.*, 2011, **158**(5), p 118–124.
10. M. Arab, M. Azadi and O. Mirzaee, Effects of Manufacturing Parameters on the Corrosion Behavior of Al-B$_4$C Nanocomposites, *Mater. Chem. Phys.*, 2020 https://doi.org/10.1016/j.matchemphys.2020.123259
11. K.K. Alaneme and P.A. Olubambi, Corrosion and Wear Behaviour of Rice Husk Ash-Alumina Reinforced Al-Mg-Si Alloy Matrix Hybrid Composites, *J. Mater. Res. Technol.*, 2013, **2**(2), p 188–194.
12. N. Ashrafi, M.A. Azmah Hanim, M. Sarraf, S. Sulaiman and T.S. Hong, Microstructural, Tribology and Corrosion Properties of Optimized Fe$_3$O$_4$-SiC Reinforced Aluminum Matrix Hybrid Nano Filler Composite Fabricated Through Powder Metallurgy Method, *Material*, 2020 https://doi.org/10.3390/ma13184090
13. N. Abu-Warda, M.D. López, M.D. Escalera-Rodríguez, E. Otero and M.V. Utrilla, Corrosion Behavior of Mechanically Alloyed A6005 Aluminum Alloy Composite Reinforced with TiB$_2$ Nanoparticles, *Mater. Corros.*, 2019, **7**, p 1–10.
14. H. Mindivan, Reciprocal Sliding Wear Behaviour of B$_4$C Particulate Reinforced Aluminum Alloy Composites, *Mater. Lett.*, 2010, **64**(3), p 405–407.
15. M. Alizadeh, M. Alizadeh and R. Amini, Structural and Mechanical Properties of Al/B$_4$C Composites Fabricated by Wet Attrition Milling and Hot Extrusion, *J. Mater. Sci. Technol.*, 2013, **29**(8), p 725–730.
16. Z. Doni, A.C. Alves, F. Toptan, J.R. Gomes, A. Ramalho, M. Buciumeanu, L. Palaghian and F.S. Silva, Dry Sliding and Tribocorrosion Behaviour of Hot Pressed CoCrMo Biomedical Alloy as Compared with the Cast CoCrMo and Ti6Al4V Alloys, *Mater. Des.*, 2013, **52**, p 47–57.
17. T. Varol and A. Canakci, Effect of Weight Percentage and Particle Size of B$_4$C Reinforcement on Physical and Mechanical Properties of Powder Metallurgy Al2024-B$_4$C Composites, *Met. Mater. Int.*, 2013, **19**(6), p 1227–1234.
18. M. Nagaral, B.K. Shivananda, V. Auradi and S.A. Kori, Development and Mechanical-Wear Characterization of Al2024-Nano B$_4$C Composites for Aerospace Applications, *Strength Fract. Comp.*, 2020, **13**, p 1–13.
19. L. Zhang, Z. Wang, Q. Li, J. Wu, G. Shi, F. Qi and X. Zhou, Microtopography and Mechanical Properties of Vacuum Hot Pressing Al/B$_4$C Composites, *Ceram. Int.*, 2018, **44**, p 3048–3055.
20. A. Monshi, M. Reza Foroughi and M. Reza Monshi, Modified Scherrer Equation to Estimate More Accurately Nano-Crystallite Size using XRD, *World J. Nano Sci. Eng.*, 2012, **2**, p 154–160.
21. S.O. Akinwamide, B.T. Abe, O.J. Akinribide, B.A. Obadele and P.A. Olubambi, Characterization of Microstructure, Mechanical Properties and Corrosion Response of Aluminium-Based Composites Fabricated Via Casting—A Review, *Int. J. Adv. Manuf. Tech.*, 2020, **109**, p 975–991.
22. W. Hubner, G. Wranglen, *Current Corrosion Research in Scandinavia, Lectures held at 4th Scandinavian Corrosion Congress*, 1964, p 60–69
23. M. Tayebi, M. Jozdani and M. Mirhadi, Thermal Expansion Behavior of Al-B$_4$C Composites by Powder Metallurgy, *J. Alloys Compd.*, 2019 https://doi.org/10.1016/j.jallcom.2019.151753
24. Q. Bai, L. Zhang, L. Ke, P. Zhu, Y. Ma, S. Xia and B. Zhou, The Effects of Surface Chemical Treatment on the Corrosion Behavior of an Al-B$_4$C Metal Matrix Composite in Boric Acid Solutions at Different Temperatures, *Corros. Sci.*, 2020 https://doi.org/10.1016/j.corsci.2019.108356
25. Y. Zhang, Q. Wang, G. Chen and C.S. Ramachandran, Mechanical, Tribological and Corrosion Physiognomies of CNT-Al Metal Matrix Composite (MMC) Coatings Deposited by Cold Gas Dynamic Spray (CGDS) Process, *Surf. Coat. Tech.*, 2020 https://doi.org/10.1016/j.surfcoat.2020.126380
26. L.H. Hihara and R.M. Latanision, Corrosion of Metal Matrix Composites, *Int. Mater. Rev.*, 1994, **39**, p 245–264.
27. K.D. Ralston, D. Fabijanic and N. Birbilis, Effect of Grain Size on Corrosion of High Purity Aluminium, *Electrochim. Acta*, 2011, **56**, p 1729–1736.
28. W.R. Osorio, C.M. Freire and A. Garcia, The Role of Macrostructural Morphology and Grain Size on the Corrosion Resistance of Zn and Al Castings, *Mat. Sci. Eng. A*, 2005, **402**, p 22–32.
29. T.G. Durai, K. Das and S. Das, Effect of Mechanical Milling on the Corrosion Behaviour of Al-Zn/Al$_2$O$_3$ Composite in NaCl Solution, *J. Mater. Sci.*, 2007, **42**, p 8209–8214.
30. P. Ponthiaux, F. Wenger, D. Drees and J.P. Celis, Electrochemical Techniques for Studying Tribocorrosion Processes, *Wear*, 2004, **256**, p 459–468.
31. J. Pu, J. Wang, D. He and S. Wan, Corrosion and Tribocorrosion Behaviour of Super-Thick Diamond-Like Carbon Films Deposited on Stainless Steel in NaCl Solution, *Surf. Interface Anal.*, 2016, **48**, p 360–367.
32. A.C. Fernandes, F. Vaz, E. Ariza, L.A. Rocha, A.R.L. Ribeiro, A.C. Vieira, J.P. Rivière and L. Pichon, Tribocorrosion Behaviour of Plasma Nitrided and Plasma Nitrided + Oxidised Ti6Al4V Alloy, *Surf. Coat. Tech.*, 2006, **200**, p 6218–6224.
33. M. Azzi, M. Paquette, J.A. Szpunar, J.E. Klemberg-Sapieha and L. Martinu, Tribocorrosion Behaviour of DLC-Coated 316L Stainless Steel, *Wear*, 2009, **267**, p 860–866.
34. F. Mindivan and H. Mindivan, Surface Properties and Tribocorrosion Behaviour of a Thermal Sprayed Martensitic Stainless Steel Coating after Pulsed Plasma Nitriding Process, *Adv. Mater. Proces. Technol.*, 2016, **2**(4), p 514–526.
35. B. Rebba and N. Ramanaiah, Investigations on Mechanical Behaviour of B$_4$C and MoS$_2$ Reinforced AA2024 Hybrid Composites, *J. Manuf. Sci. Prod.*, 2015, **15**(4), p 339–343.
36. C.R. Kumar, R.R.R. Malarvannan and V. JaiGanesh, Role of SiC on Mechanical, Tribological and Thermal Expansion Characteristics of B$_4$C/Talc-Reinforced Al-6061 Hybrid Composite, *SILICON*, 2020, **12**, p 1491–1500.
37. A. Radha, S. Suresh, G. Ramanan, V. Mohanavel and C.E. Prema, Processing and Characterization of Mechanical and Wear Behavior of Al7075 Reinforced with B$_4$C and Nano Graphene Hybrid Composite, *Mater. Res. Express*, 2020 https://doi.org/10.1088/2053-1591/ab6263